Constructing molybdenum vacancy defect for MoP with optimized p-band center towards high-efficiency hydrogen evolution

Ting Guo [a], Hao Fei [a], Ruoqi Liu [a], Fangyang Liu [b], Dezhi Wang [a], Zhuangzhi Wu [a],[*]

[a] School of Materials Science and Engineering, Central South University, Changsha 410083, China
[b] School of Metallurgy and Environment, Central South University, Changsha 410083, China

ABSTRACT

Vacancy engineering has been widely used to enhance the hydrogen evolution reaction (HER) performance due to its effective electronic modulation effect. Herein, the molybdenum (Mo) vacancies were introduced into molybdenum phosphide (MoP) towards high-efficiency hydrogen evolution for the first time. Benefiting from the charge redistribution around the Mo vacancies, the exposed P sites can serve as ideal catalytic sites with a free energy of hydrogen adsorption close to zero. Meanwhile, an internal polarization field from terminal Mo atoms to exposed P atoms can offer a more efficient "H delivery" mechanism, achieving fast HER kinetics with a dominant Volmer-Heyrovsky mechanism at a wide range of current density and ultimately exceeding the commercial Pt/C catalyst for high-efficiency hydrogen evolution. More importantly, we first report that the P p-band center can be used as an alternative descriptor to evaluate the HER performance of the electrocatalysts which utilize P atoms as the main active sites. Furthermore, this work also demonstrates that metal vacancies provide an effective tactic to optimize catalytic activity for metal compound-based electrocatalysts.

1. Introduction

Vacancy, distinguished as a sort of unique catalytic active sites, has been widely investigated in the hydrogen evolution reaction (HER), due to its efficient electronic modulation effect over a broad range [1–6]. At present, numerous vacancy engineering tactics, such as low-temperature hydrothermal growth [7–9], gas plasma bombardment [10–13], etching [1,4,14,15], and heteroatom doping [16–18], have been proposed to optimize HER performances. Specifically, as regards to the molybdenum-based materials, recognized as promising HER electrocatalysts, the prevalent strategy is etching. Sulfur (S) vacancy has been widely utilized to activate the inert basal plane of molybdenum disulfide (MoS_2). Wang and Zhang et al. used hydrogen peroxide as a mild chemical etchant for introducing single S-vacancies onto the MoS_2 nanosheet surface, and the S-vacancy state can be systematically modulated by tuning the etching duration, temperature, and solution concentration [1]. Besides, oxygen (O) vacancy has been introduced into the catalytically inactive molybdenum trioxide (MoO_3) to achieve remarkable HER performance. Luo and Suib et al. employed poly-ethylene oxide-*b*-polystyrene (PEO-*b*-PS) as soft template as well as reducing agent for etching O-atoms from MoO_3, and the O-vacancies not

only served as electron acceptors reducing the HER kinetic barrier, but also enhanced the electrical conductivity [19]. For the low oxidation state molybdenum-based materials, cation vacancy is preferable for the acceleration of HER because of the strong Mo–H bond. Li and Baek et al. utilized silicon dioxide as the hard template to create Mo vacancies on the surface of molybdenum carbide (Mo_2C) during template etching, and the Mo vacancies would weaken the Mo–H bond as confirmed by the density functional theory (DFT) calculations [14]. Molybdenum phosphide (MoP) is acknowledged as the most efficient HER electrocatalyst among molybdenum-based materials on account of its high intrinsic activities [20], but there is few research on the vacancy-rich MoP electrocatalyst. Since Xiao and Wang et al. discovered molybdenum phosphides as promising HER electrocatalysts for the first time [21], P atoms have been considered as active sites with optimal Gibbs free energy of hydrogen adsorption (ΔG_{H^*}, −0.03 eV at 2/4 mL), whereas Mo atoms exhibited too strong binding to H. However, when the H coverage was increased to 3/4 mL, the ΔG_{H^*} of P terminated surface reached a much higher value of 0.34 eV, it meant that high surface H coverage as well as corresponding fast Heyrovsky reaction kinetics were difficult to be achieved. Based on the above discussion, constructing Mo vacancy defect for MoP may be a rational and effective strategy to expose more P

* Corresponding author.
  E-mail address: zwu@csu.edu.cn (Z. Wu).

active sites as well as increase the H coverage of defective surface.

Herein, the molybdenum vacancies were introduced into MoP through an etching process for the first time. As shown in Fig. 1, Co_2P/MoP nanorods were obtained firstly by the phosphorization of the $CoMoO_4$ precursor, during which abundant Co−P−Mo bonds were established at the interface between Co_2P and MoP. Afterwards, the Co_2P crystalline phase was etched by the hydrochloric acid easily, resulting in a large number of molybdenum vacancies derived from the destruction of Mo−P−Co linker. DFT calculation results indicated that the molybdenum vacancies not only facilitated the exposure of P atoms giving a ΔG_{H*} close to zero for hydrogen evolution, but also constructed an internal polarization field from terminal Mo atoms to exposed P atoms, enabling a higher surface coverage of H as well as corresponding faster Heyrovsky reaction kinetics. As expected, the Mo vacancy-rich MoP exhibited accelerated HER kinetics with an ultralow Tafel slope of 41 mV dec^{-1}. Moreover, we further probed the correlation between P p-band center (ε_p) and ΔG_{H*} of a series of molybdenum phosphide-based electrocatalysts, and first reported the P ε_p could be used as an alternative descriptor to evaluate the HER performance. This work not only paves a new avenue for the rational design and construction of phosphide-based HER electrocatalysts, but also provides an efficient tactic to optimize catalytic activity for other metal compound-based electrocatalysts which rely on non-metal atoms as main catalytic sites.

2. Experimental section

2.1. Synthesis of CoMoO₄ nanorods

The $CoMoO_4$ nanorods were synthesized via a hydrothermal method. In brief, $Co(NO_3)_2 \cdot 6 H_2O$ (2 mmol) and $Na_2MoO_4 \cdot 2 H_2O$ (2 mmol) were dissolved in deionized water (40 mL), and then transferred into a Teflon-lined stainless-steel autoclave (100 mL) and maintained at 180 °C for 12 h. After being cooled to room temperature, the purple $CoMoO_4$ powder was collected by filtration and washing with water and ethanol as well as being dried at 70 °C overnight. XRD and SEM characterizations were conducted for the as-obtained $CoMoO_4$ precursor (Fig. S1). The XRD pattern of precursor synthesized by the hydrothermal reaction can be indexed as the phase for $CoMoO_4 \cdot 3/4 H_2O$. After one hour of calcination at 500 ℃, the diffraction peaks matched well with the monoclinic $CoMoO_4$ (PDF#21-0868) [22]. And SEM images revealed a typical nanorod structure.

2.2. Synthesis of Co₂P/MoP nanorods

The Co_2P/MoP nanorods were prepared via a high temperature phosphorization method. In brief, the as-obtained $CoMoO_4$ nanorods (50 mg) and $NaH_2PO_2 \cdot H_2O$ (125 mg) were dispersed into two porcelain boats with the latter on the upstream side. Then, the furnace was heated at 600 °C in the Ar gas flow for 1 h with a ramp rate of 10 °C min^{-1}.

2.3. Synthesis of Mo vacancy-rich MoP porous nanorods

The Mo vacancy-rich (Mov) MoP porous nanorods were obtained through HCl etching of the Co_2P/MoP nanorods. In brief, the Co_2P/MoP (20 mg) nanorods were dispersed into 1 M HCl solution (100 mL) under vigorous stirring for hours, and the final sample was collected by filtration and washed with water and ethanol, named as Mov-MoP-*t* (*t* is the etching time).

2.4. Synthesis of pristine MoP nanorods

The pristine MoP (P-MoP) nanorods were obtained through the same method as for Co_2P/MoP nanorods but replacing $CoMoO_4$ nanorods with MoO_3 nanorods and increasing the calcination temperature to 700 °C. The obtained P-MoP nanorods were also subjected to an 18-hour acid etching with 1 M HCl, named as P-MoP-18.

2.5. Characterizations

XRD patterns were obtained by a D/max 2500 system with a Cu Kα radiation source. Zeiss Sigma 300 scanning electron microscope (SEM) and FEI Tecnai F20 transmission electron microscope (TEM) were utilized to observe the morphology and microstructures. The contact angle was determined by Lauda Scientific LSA100. The surface elemental valence states were measured by both X-ray photoelectron spectrometer (XPS, Thermo Fisher Scientific K-ALPHA) and electron paramagnetic resonance spectrometer (EPR, Bruker EMXplus-6/1). The valance bands were measured by ultraviolet photoelectron spectroscopy (UPS, Kratos Axis Ultra HSA).

3. Results and discussion

To investigate the formation process of Mo vacancy, a series of Mo vacancy-rich samples were prepared via the phosphorization of as-obtained $CoMoO_4$ precursors followed by HCl etching. As shown in Fig. 2a, the diffraction peaks of pristine Co_2P/MoP (P-Co_2P/MoP) match well with the standard Co_2P (PDF#32-0306) and MoP (PDF#65-6487) [23,24], demonstrating the complete phosphorization of as-obtained $CoMoO_4$ precursors. With the increase of etching time, the characteristic peak at 39.5° corresponding to the (201) plane of orthorhombic
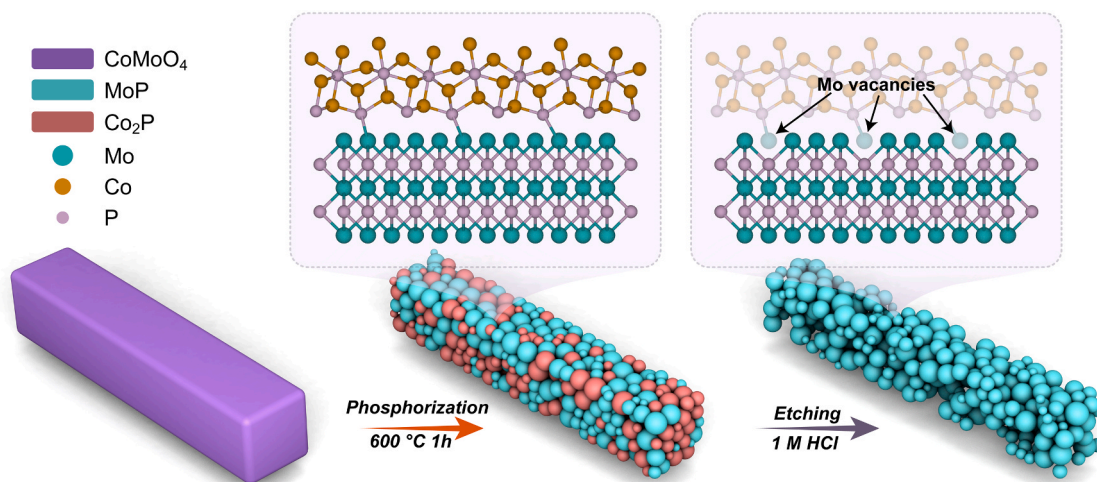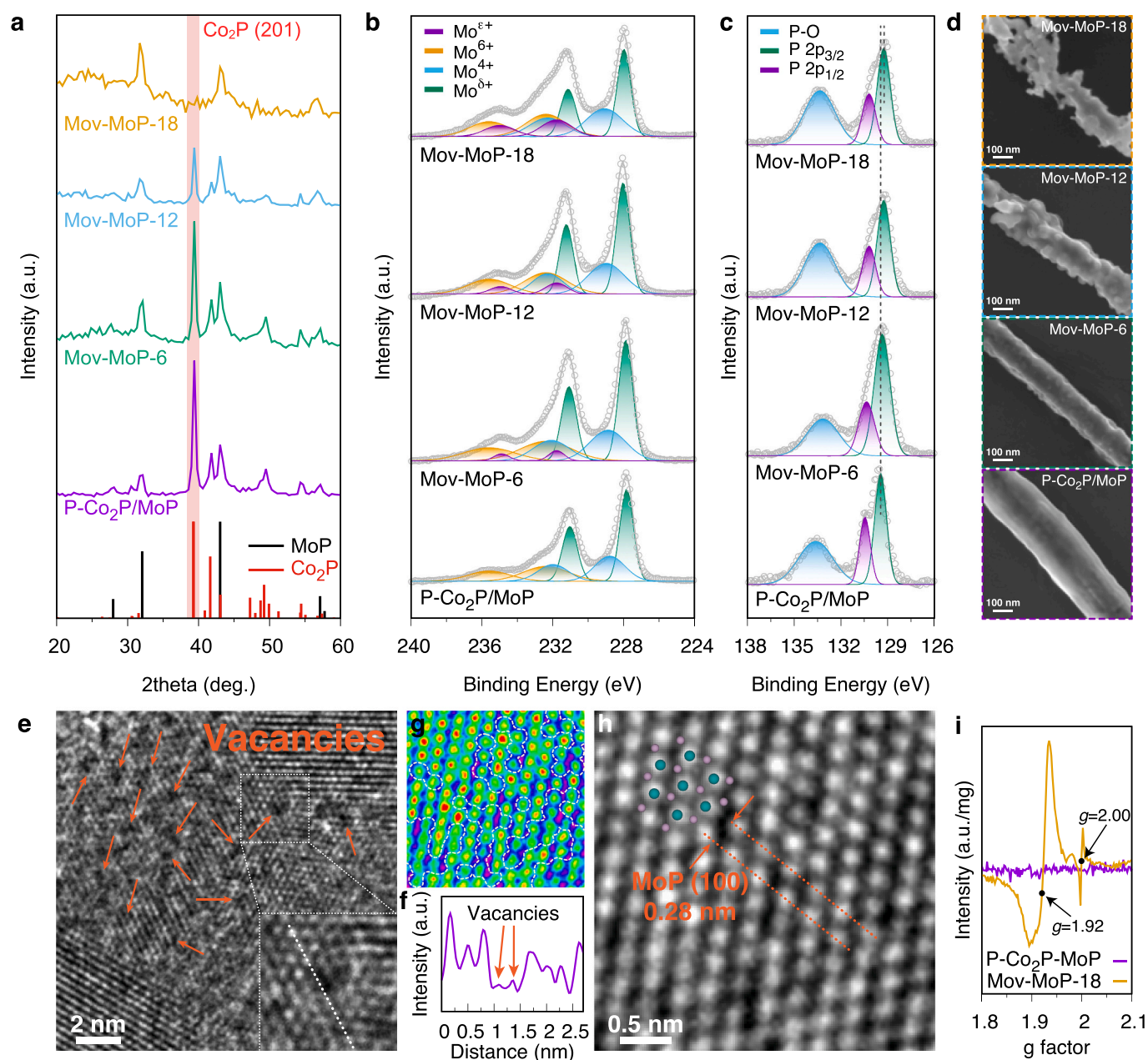

Fig. 1. Schematic representation for the preparation of Mo vacancy-rich MoP electrocatalyst.

Fig. 2. Composition, surface chemical and morphology characteristics of P-Co$_2$P/MoP, P-MoP and Mov-MoP-*t*. (a) XRD patterns. (b) Mo 3d XPS spectra. (c) P 2p XPS spectra. (d) SEM images. (e-h) TEM and HR-TEM images of Mov-MoP-18. (i) EPR spectra.

Co$_2$P is weakened gradually until disappears completely after HCl etching for 18 h. Moreover, no obvious shift is observed for the main diffraction peak at 43.0° corresponding to (101) plane of hexagonal MoP comparing with the standard pattern, implying that no Co atom is replaced or inserted into the MoP crystal.

To further explore the changes of elemental chemical states after HCl etching, X-ray photoelectron spectroscopy (XPS) measurements were conducted. Fig. 2b shows the high-resolution Mo 3d spectra. For P-Co$_2$P/MoP, the Mo 3d spectrum can be deconvoluted into four doublet peaks with a fixed spin energy separation of 3.20 eV, and the main doublet located at 227.85 and 231.05 eV can be assigned to the Mo$^{\delta+}$ ($0 < \delta < 4$) species from MoP, the rest of Mo species with higher oxidation states (Mo^{4+} and Mo^{6+}) should be attributed to the inevitable surface oxidation upon exposure to air [25]. With the continuous HCl etching, the ratio of Mo$^{\delta+}$ species is decreased gradually (detailed information is provided in the Supporting Information, Table S1), indicating the

breaking of Mo−P bonds derived from the destruction of Mo−P−Co linker in the etching process as shown in Fig. 1. Moreover, interestingly, a new doublet located between Mo^{4+} and Mo^{6+} denoted as Mo$^{\epsilon+}$ ($4 < \epsilon < 6$) can be observed. Because no obvious enhancement is observed for Mo^{4+} and Mo^{6+} species, the emerging Mo$^{\epsilon+}$ species should not be ascribed to more serious surface oxidation. Meanwhile, the high-resolution O 1 s spectra in Fig. S2 (Supporting Information) also prove that no evident increase of lattice oxygen (O^{2-}) or highly oxidative oxygen (O$_2^{2-}$/O$^-$) species are detected for Mov-MoP-*t* [26]. Consequently, the new Mo$^{\epsilon+}$ species should be caused by constructing agglomerate Mo vacancies, forming localized Mo$_{1-x}$P phase in the etching process. The high-resolution P 2p spectra (Fig. 2c) depict a doublet at 129.50 and 130.50 eV corresponding to the metal-P bonds [27,28], which shift to lower binding energy gradually with the formation of Mo vacancies, indicating that more electrons transfer to P sites from the emerging Mo$^{\epsilon+}$ species [29]. Finally, the high-resolution Co 2p

spectra (Fig. S3) were also investigated to study the variations in Co element in the samples before and after etching treatment [4], as etching time increased, the peak intensity of the cobalt element gradually diminished, and no signal was observed in Mov-MoP-18, which suggests that most of the Co species were eliminated by the HCl etching treatment after 18 h.

Ultraviolet photoelectron spectroscopy (UPS) was conducted to further confirm the surface electron transfer phenomenon resulting from Mo vacancies. Fig. S4 shows the UPS spectra of valance band near to the Fermi level (E_F), and a new peak at 2.9 eV can be detected on the Mov-MoP-18 surface, indicating more electrons gathering around the E_F [4, 30]. In brief, with the construction of Mo vacancies, more electrons transfer to P sites and result in the increased valance electron concentration around E_F, finally enhancing the chemisorption capacity toward H for P atoms [31].

The formation of porous structure in the HCl etching process was observed by the scanning electron microscopy (SEM), as shown in Fig. 2d. The monodisperse P-Co$_2$P/MoP nanorod presents the same smooth surface as the CoMoO$_4$ precursor (Fig. S1b). With the continuous etching treatment, the porous structure appears gradually on account of the elimination of Co$_2$P nanoparticles during the etching process, which will promote the mass transfer significantly in HER. To further investigate the elemental distribution and content of Mov-MoP-18, energy-dispersive X-ray spectroscopy (EDS) analysis was performed. As shown in Fig. S5, both Mo and P elements were uniformly distributed throughout the Mov-MoP-18, but no significant cobalt element signal was detected, which is consistent with the XPS results.

Besides the porous structure, the hydrophilicity affects the mass transfer behavior which determines the kinetics of HER [32]. Fig. S6 shows the contact angles of P-MoP, Mov-MoP-18, and P-Co$_2$P-MoP, and the P-Co$_2$P-MoP exhibits the best wettability on account of the strong hydrophilicity of cobalt species [33]. Although Mov-MoP-18 shows inescapable decay due to the entire elimination of Co$_2$P, the contact angle of 51.6° is obviously smaller than that of P-MoP (63.9°). Based on the results of composition and morphology (Fig. 2a, d and Fig. S7a,e), the enhanced wettability should be mainly attributed to the interconnected porous structures [34].

To further probe the presence of Mo vacancies visually, high-resolution TEM (HR-TEM) images of Mov-MoP-18 were captured. Fig. 2e depicts discontinuous lattice fringes as well as corresponding image intensity line profiles (along the white dash line, Fig. 2f), indicating the presence of point defects, which should be attributed to Mo vacancies base on the XPS results. Besides, Fig. 2h shows the vacancy-rich spot which contains agglomerate smaller and dimmer dots (marked by light yellow dash lines in the left heat map image Fig. 2g), and typical interplanar distance of 0.28 nm can be assigned to the (100) plane of hexagonal-phase MoP (the inset illustrates the atomic model), proving the existence of agglomerate Mo vacancies on the MoP (001) plane. In addition, TEM images of Mov-MoP with different etching times were shown in Fig. S8. Distinct penetrating pore channels can be observed in Mov-MoP-12 (Fig. S8f) and Mov-MoP-18(Fig. S8k), consistent with the SEM images. All the samples exhibited structural defects such as edge dislocations, lattice distortions, and twin crystals (Fig. S8b, c, g, h, l, m), which are commonly found in nanocrystalline materials, and these structural defects were also observed in P-MoP (Fig. S7b,c). Due to the residual Co$_2$P phase in Mov-MoP-6 and Mov-MoP-12, Fig. S8d,i displayed the Co$_2$P/MoP heterojunction interface. However, in Mov-MoP-18, no matching crystal plane spacing corresponding to Co$_2$P could be found. Based on XPS results, even though the vacancy concentration was relatively low in Mov-MoP-6 and Mov-MoP-12, vacancy-rich spots on the MoP (001) crystal plane in Mov-MoP-6 and Mov-MoP-12 could still be easily observed (Fig. S8e,j). In contrast, the MoP (001) crystal plane in P-MoP exhibited much more perfect crystallinity (Fig. S7d), indicating that Co$_2$P etching was the key factor for constructing Mo vacancies.

To further verify the existence of Mo vacancies, electron

paramagnetic resonance (EPR) was performed, as shown in Fig. 2j. No obvious signal is detected for P-Co$_2$P-MoP, demonstrating its good crystalline property with negligible defects before etching. As to Mov-MoP-18, the broad signal at g = 1.92 should be ascribed to the Mo^{5+} species [35], which agrees with the XPS results. Besides, a thin characteristic signal corresponding to non-metallic radical species derived from the Mo$-$P dangling bonds can be clearly detected at g = 2.00 [35], which further confirms the successful construction of vacancy defects in Mov-MoP-18 [1].

The HER performances of Mov-MoP-t electrocatalysts were evaluated systematically to investigate the impact of Mo vacancies on HER catalytic activity. Besides, P-Co$_2$P/MoP and P-MoP were also evaluated for comparison. As shown in Fig. 3a and b, P-MoP exhibits the worst HER performance with a high overpotential of $-$ 371 mV to reach the current density (j) of 100 mA cm^{-2} (η_{100}) as well as a large Tafel slope of 60 mV dec^{-1} in 0.5 M H$_2$SO$_4$, in good agreement with the previous works [36, 37]. Although P-Co$_2$P/MoP shows a slightly better activity than P-MoP with a lower η_{100} of $-$ 339 mV and a smaller Tafel slope of 57 mV dec^{-1}, the slight improvement of catalytic activity may be mainly attributed to the increased number of active sites beneficial from the heterostructure [38]. Surprisingly, Mov-MoP only requires a much smaller η_{100} of $-$ 206 mV than P-MoP and P-Co$_2$P/MoP, and the superiority is increased continuously because of its ultralow Tafel slope of 41 mV dec^{-1}. Tafel slope is a pivotal parameter to investigate the reaction kinetics and rate-determining step (RDS) in the electrocatalytic process. Fig. 3b depicts all the as-obtained electrocatalysts exhibiting Tafel slope values between $40 - 120$ mV dec^{-1}, indicating that the Heyrovsky reaction ($M-H_{ads} + H_3O^+ + e^- \rightarrow M + H_2 + H_2O$) is the RDS in this work [4]. The ultralow Tafel slope of Mov-MoP near 40 mV dec^{-1} implies a high hydrogen coverage on the active sites with a low current density (i.e., the initial stage of HER) [39], which may be ascribed to the enhancement of Volmer reaction ($H_3O^+ + M + e^- \rightarrow M-H_{ads}$) at relative high hydrogen coverage resulting from the charge redistribution around the Mo vacancies. More detailed descriptions of the relationship between Tafel slope and current density are given in Fig. S9. The Tafel slope of Mov-MoP is not larger than 120 mV dec^{-1} until the current density exceeds 100 mA cm^{-2}, that is to say, the Volmer reaction is fast enough thus the Heyrovsky reaction is always the RDS before the current density reachs 100 mA cm^{-2}. Furthermore, although the minimal Tafel slope value of the Mov-MoP is slightly higher than that of Pt/C (31 mV dec^{-1}), at the strong polarization zone ($j = 100$ mA cm^{-2}), Mov-MoP shows a smaller Tafel slope of 119 mV dec^{-1} than that of Pt/C (176 mV dec^{-1}), which is also much lower than that of P-MoP (291 mV dec^{-1}) and P-Co$_2$P/MoP (249 mV dec^{-1}). It means that the Mov-MoP electrocatalysts are capable of driving a high current density with a smaller overpotential as well as practical applications, just as revealed in Fig. 3a, and Mov-MoP has a much smaller overpotential than Pt/C to reach the current density greater than 450 mA cm^{-2}.

In order to probe the main reason for the performance enhancement more accurately, XPS and electrochemical tests were conducted on both P-MoP and P-MoP-18 (Fig. S7f,g). Because MoP is not sensitive to acid etching, acid treatment did not affect the surface chemical states of MoP. In comparison to Mov-MoP-18, no Mo$^{\varepsilon+}$ ($4 < \varepsilon < 6$) species could be observed for both P-MoP and P-MoP-18, indicating that no molybdenum vacancy was constructed, consistent with TEM results. Similarly, P-MoP-18 showed no significant difference in hydrogen evolution catalytic performance compared to P-MoP. Combining the results from XPS, TEM, and electrochemical tests, it can be concluded that Mo vacancies are the primary factor contributing to the significant improvement in hydrogen evolution catalytic performance for Mov-MoP-18, and the construction of Mo vacancies is closely associated with the etching process of Co$_2$P.

To further explore the optimization mechanism of vacancy engineering in this work, the Mov-MoP electrocatalysts with different etching time were also assessed and shown in Fig. S10a-d and Table S2. More visualized histogram is depicted in Fig. 3c, in which distinct improvement of electrochemical performance, including η_{100}, Tafel
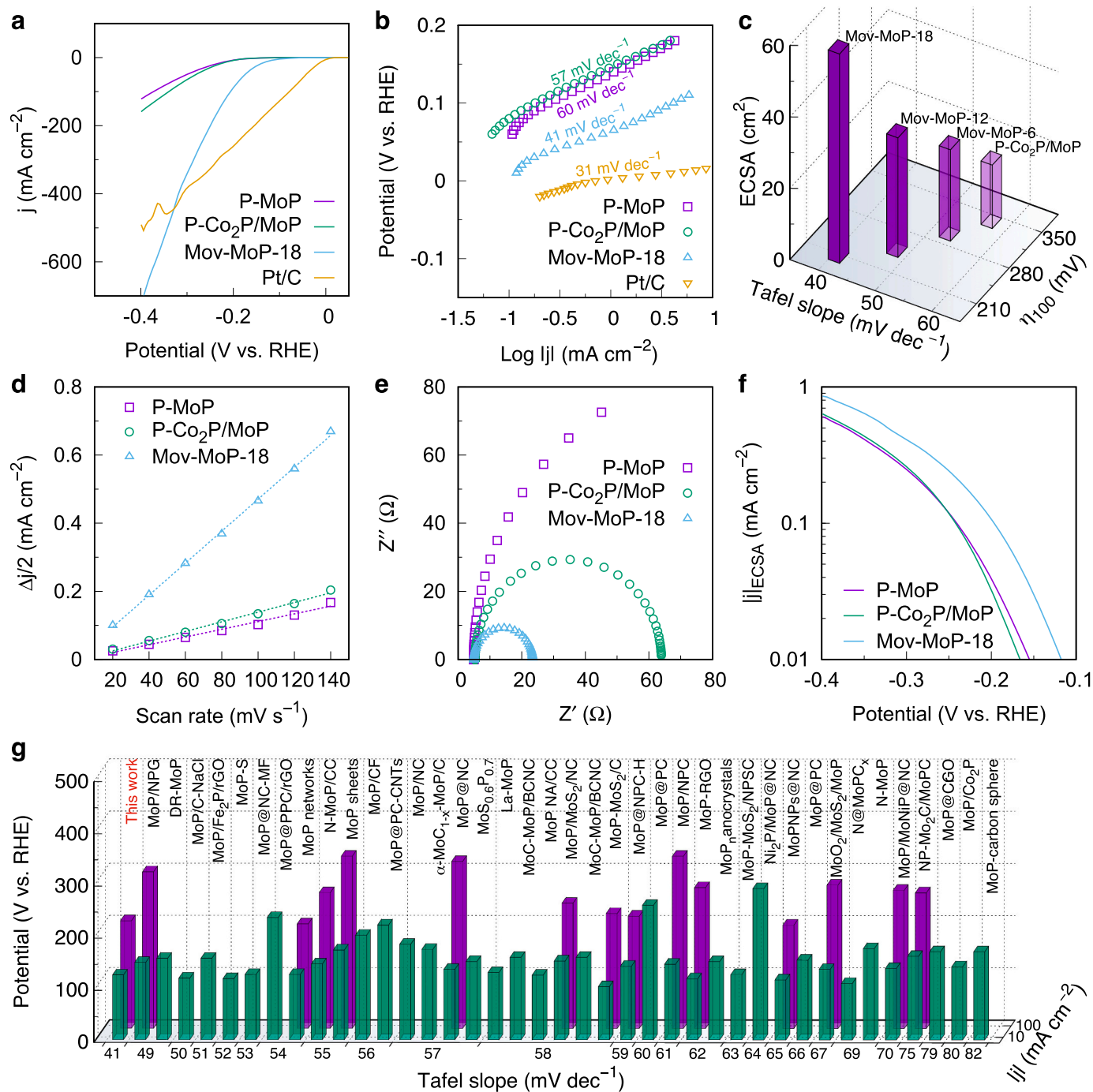
Fig. 3. HER performances of P-Co₂P/MoP, Mov-MoP and P-MoP in 0.5 M H₂SO₄. (a) Polarization curves (without iR-correction). (b) Tafel plots. (c) Comparison of Tafel slope, η_{100} and ECSA for Mov-MoP-*t*. (d) Measured capacitive currents plotted as a function of the scan rate. (e) Nyquist plots. (f) Polarization curves normalized by ECSA. (g) Comparison of Mov-MoP with other reported MoP-based electrocatalysts (The green and purple histogram represent the overpotential when the current density reaches 10 and 100 mA cm⁻² respectively).

slope and ECSA, can be observed with the continuous increase of etching time, and the Mov-MoP-18 presents the optimal HER performance ultimately. Specifically, the Mo vacancy not only can improve the intrinsic activity by accelerating the HER kinetics, but also maximize the active sites by promoting the exposure of active P atoms as well as constructing porous structures. Moreover, electrochemical impedance spectroscopy (EIS) gives the charge transfer resistance (R_ct) fitted by the corresponding equivalent circuit (Fig. S11). Similar to the results of Tafel plots, the R_ct values of Mov-MoP-*t* obviously show a downward trend as the increased HCl etching time, confirming the accelerated HER kinetics

of Mov-MoP electrocatalysts again. As the etching time is further increased to 24 h, no significant change in the HER performance is observed (Fig. S12a). XRD, XPS and SEM were performed to investigate the difference of composition and morphology between Mov-MoP-18 and Mov-MoP-24 (Fig. S12b-d), and it is found that continuous etching treatment will not cause any distinct modification over the sample if most of the Co₂P particles have already been eliminated.

The ECSA and EIS of P-MoP were also measured, as shown in Fig. 3d, e and Table S2. Detailed calculations about electrochemical surface area (ECSA) are shown in Supporting Information. P-Co₂P/MoP possesses a

slightly larger ECSA and faster charge transfer rate than P-MoP, consisting with the speculation that the heterostructure increases the active site density. As expected, Mov-MoP gets a much higher ECSA ($58.65\ cm^2_{ECSA}$) and lower R_{ct} ($18.4\ \Omega$) than those of P-MoP ($14.17\ cm^2_{ECSA}$ and $171.2\ \Omega$, respectively), further confirming the superiority of Mov-MoP. To evaluate the specific HER activity precisely, the current density was normalized by the corresponding ECSA (Fig. 3f). Encouragingly, Mov-MoP still depicts the highest value, demonstrating the effective optimization of inherent activity by constructing Mo vacancies. Whereas, P-Co$_2$P/MoP only shows an inferior value similar to that of P-MoP, implying that the Co$_2$P species are not very active for the acidic HER in this work.

Fig. 3g and Table S4 depict the comparison of Mov-MoP with other reported MoP-based electrocatalysts. Evidently, most MoP-based electrocatalysts exhibit relatively sluggish HER kinetics with Tafel slopes greater than 50 mV dec^{-1}, which also consist with the electrochemical results of P-MoP in this work. Whereas the Tafel slope of Mov-MoP (41 mV dec^{-1}) is far smaller than those of MoP-based electrocatalysts, and its superiority of HER activity would further increase under higher potentials just as revealed in the discussion about Fig. S9.

Besides in acidic media, the as-obtained electrocatalysts were also investigated in 1 M KOH (Fig. S10e-l and Table S3). Although Mov-MoP still possesses superior HER kinetics with an ultralow Tafel slope of 41 mV dec^{-1} as the same as that in acidic media, Co$_2$P species play an important role in alkaline solution. Not only P-Co$_2$P/MoP exhibits preferable HER electrocatalytic performance than P-MoP distinctly, but also the Mov-MoP-12 with both Co$_2$P/MoP heterojunction and Mo vacancies shows higher activity than Mov-MoP-18 in which most of the Co species have been eliminated, despite Mov-MoP-18 possesses higher density of active sites. The significant influence of Co$_2$P on HER activity in alkaline solution should be ascribed to its strong hydrophilicity (Fig. S6) as well as low energy barrier of water dissociation on the Co atoms [40].

Stability is also an important performance indicator for the HER. It is well known that Co$_2$P is soluble under acidic conditions. During the chronoamperometric test of Co$_2$P/MoP under acidic conditions (Fig. S16), the current density gradually increased with the testing time. Based on the previous analysis, the enhanced HER performance should be attributed to the continuous dissolution of Co$_2$P, leading to the construction of molybdenum vacancies and exposure of highly active P sites. Meanwhile, the structural stability issue arising from the continuous dissolution of Co$_2$P is manifested after 6 h. The abrupt decrease in current density should be ascribed to the formation of numerous in situ pores on the surface of the working electrode caused by the dissolution of Co$_2$P. Under the continuous impact of H$_2$ gas bubble, the structure collapses and detaches, ultimately resulting in a reduction of the active mass. In contrast, the Mov-MoP electrocatalyst exhibits excellent stability under both acidic and alkaline media (Fig. S17). After cyclic voltammetry for 2000 cycles, the as-obtained polarization curve is still similar to the initial one. Furthermore, during the 30-hour chronoamperometric test, no significant decay in current density can be observed. The results of XRD, XPS, and SEM characterization of the Mov-MoP-18 undergoing 30-hour chronoamperometric test in 0.5 M H$_2$SO$_4$ are shown in Fig. S17c-e, and no obvious changes in the composition and structure could be observed. These results demonstrate the excellent durability of Mov-MoP electrocatalysts, making them promising candidates for extended periods of HER applications.

In one word, the remarkable enhancement of HER performance after HCl etching should be attributed to the synergistic effect of electronic modulation and exposure of more active P sites by constructing Mo vacancies, which optimizes the intrinsic activity and active site density at the same time.

DFT calculations were then performed to unveil the optimization mechanism of Mo vacancies comprehensively. Firstly, P atoms have been acknowledged as main active sites in MoP for HER, and the degrees of phosphorization play a significant role in the HER activities [21].

Hence, the P ε_p was investigated as a significant descriptor to explore the adsorption/desorption kinetics in HER of MoP-based materials in an analogous role as the d-band center for noble metal catalysts [41,42]. To probe the influence of Mo vacancies on ε_p as well as the relationship between ε_p and phosphorization degree, four representative models with different phosphorus contents, namely, Mo$_3$P, MoP, Mov-MoP and MoP$_2$ were constructed for projected density of states (pDOS) calculations (detailed model structures are provided in the Supporting Information). As shown in Fig. 4a, an uplifted ε_p value is observed for the Mov-MoP model in contrast with the MoP model, implying enhanced Mo−P hybridization with increased molybdenum oxidation, which is supported by the above-mentioned XPS and UPS analysis [43]. The enhanced Mo−P hybridization can be also reflected by the deformation charge density and corresponding plane-averaged electron density, as depicted in Fig. 4b. The calculated isosurface of deformation charge density indicates that the electrons mainly locate around Mo−P bonds, and with the construction of Mo vacancies, more electrons prefer to accumulate around the adjacent P atoms, leaving a higher bonding electron density nearby. To be precise, the enhanced bonding electron density can facilitate the hydrogen adsorption reaction, thereby increasing the H coverage [44–46].

Furthermore, Gibbs free energy of H* adsorption, one acknowledged descriptor for evaluating the catalytic activity, was calculated as well. For the MoP model, two different (001) surfaces, namely, MoP-Mo-t with Mo terminal surface and MoP-P-t with P terminal surface were selected [47]. It is well known that P terminal atoms from MoP play a crucial role in active sites via a hydrogen delivery mechanism, whereas, Mo terminal atoms show poor activity owing to its stronger binding to H [21]. Specifically, as depicted in Fig. 4c, the ΔG_{H*} of MoP-P-t changes from −0.53 eV to 0.45 eV when the H coverage is increased from 1/4 to full coverage, implying that P atoms could adsorb H$^+$ spontaneously at the initial stage of HER (i.e., Volmer step) while release H* intermediate easily at relative high coverages (i.e., Heyrovsky step), which enables P atoms to serve as a competent H deliverer. However, a positive ΔG_{H*} of MoP-P-t at relative high H coverages means no sufficient H* intermediate for the Heyrovsky reaction, leading to large Tafel slopes (Fig. 3b). As expected, MoP-Mo-t possesses a strong Mo−H bonding with much more negative ΔG_{H*} range from −0.58 eV to −0.50 eV at various H coverages, which are beneficial to adsorb H$^+$, but at the same time hinder the desorption step. With the construction of Mo vacancies on the Mo terminal surface, although H$^+$ is preferably adsorbed on Mo atoms firstly with even more negative ΔG_{H*} than MoP-Mo-t, the exposed P atoms would serve as highly active sites with slightly negative ΔG_{H*} when Mo atoms are covered with H*. More importantly, Mo vacancies would reduce the overall electron density of Mo terminal surface, resulting a top-down-direction internal polarization field (IPF) (Fig. 4d). Such an IPF would offer a proton spillover orientating from Mo terminal atoms (H$^+$ adsorbed sites) to exposed P atoms (H* intermediate desorbed sites) [48], thereby, constructing a novel hydrogen delivery mechanism which maintains a relatively high H coverage for exposed P active sites as illustrated in Fig. 4d, boosting the Volmer and Heyrovsky reactions simultaneously.

To get a better understanding of the correlation between ΔG_{H*} and p-band electronic structures of phosphide-based electrocatalysts, the ΔG_{H*} of Mo$_3$P and MoP$_2$ with P terminal surface were also calculated. It is clear that the ΔG_{H*} of P site in Mo$_3$P and MoP$_2$ models are variable at different H coverages, but Mo$_3$P shows much larger values than zero, whereas MoP$_2$ exhibits very negative ΔG_{H*}. Inspiringly, a perfectly linear relationship between ε_p and ΔG_{H*} at full coverages can be established (Fig. 4e). Mov-MoP shows a ΔG_{H*} value close to 0 (−0.0148 eV), and the corresponding ε_p value of −2.67 eV can serve as an ideal HER performance evaluation descriptor for the electrocatalysts in which P atoms are utilized as main active sites in an analogous role as the d-band center for noble metal electrocatalysts [49].

According to the HER performances in alkaline electrolytes, a certain number of cobalt atoms can significantly improve the HER activity,
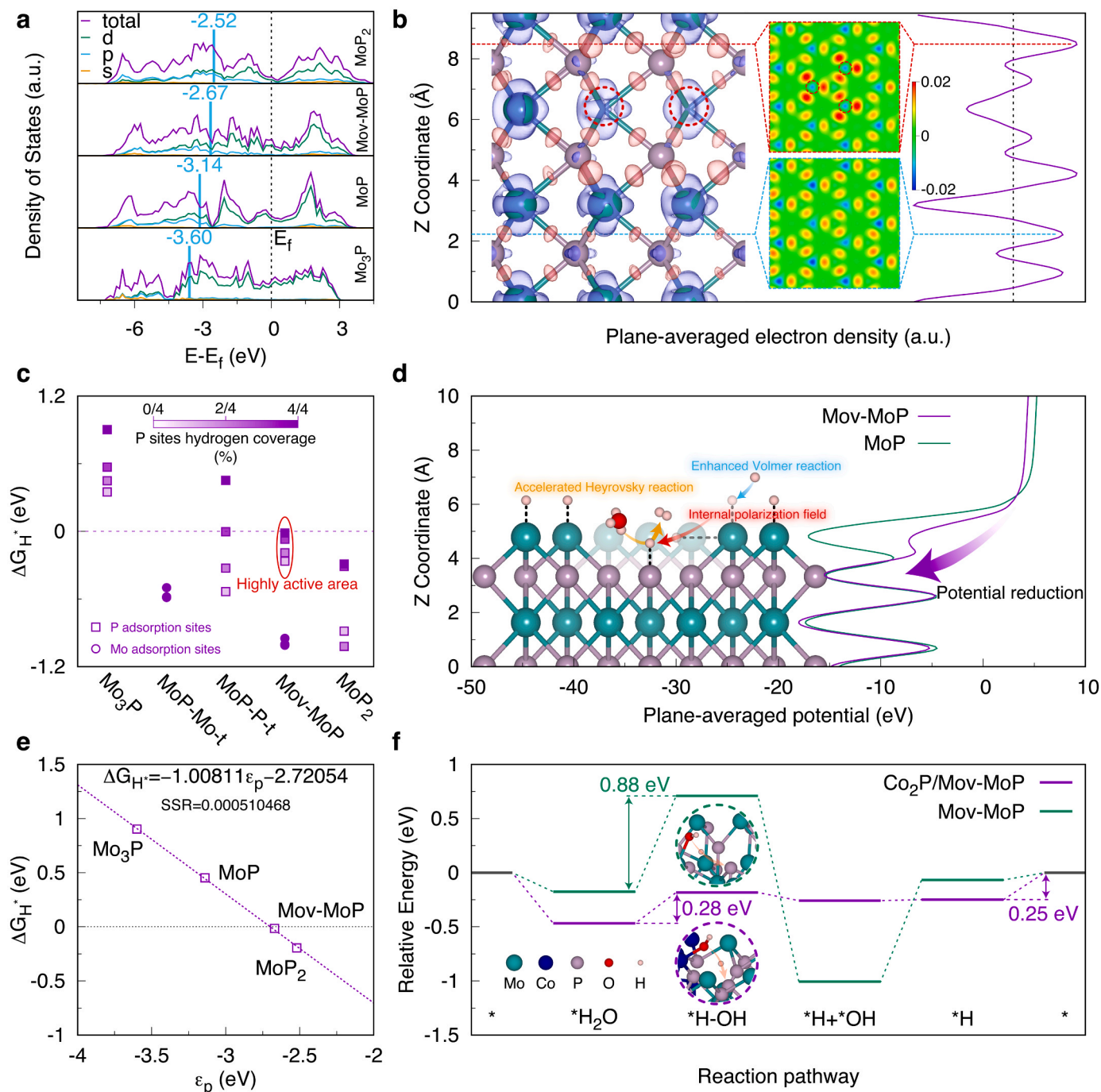
Fig. 4. (a) pDOS and relative ε_p of Mo$_3$P, MoP, Mov-MoP and MoP$_2$. (b) Deformation charge density and corresponding plane-averaged electron density, the red and blue contours represent charge accumulation and dilution, respectively. (c) ΔG_{H^*} of Mo$_3$P, MoP-Mo-t, MoP-P-t, Mov-MoP and MoP$_2$ at different H coverages. (d) Plane-averaged potential of Mov-MoP and MoP along the Z-direction and illustration of a novel hydrogen delivery mechanism via internal polarization field. (e) Linear relationship between ε_p and ΔG_{H^*}. (f) Relative energy diagram of water dissociation on Co$_2$P/Mov-MoP and Mov-MoP.

possibly due to the excellent water dissociation ability of cobalt atoms. Therefore, we performed transition state calculations for the water dissociation process of Mov-MoP and Co$_2$P/Mov-MoP (Fig. 4 f). For Co$_2$P/Mov-MoP, the Co site at the heterojunction interface was selected as the adsorption site for water dissociation, while for Mov-MoP, the Mo metal site was also identified as the adsorption site. P atoms near Mo vacancies served as active sites for hydrogen evolution in both cases. Obviously, the Co$_2$P/Mov-MoP possesses much lower water dissociation energy barrier (0.28 eV) than Mov-MoP (0.88 eV), although it exhibits a more negative ΔG_{H^*} (−0.25 eV).

4. Conclusions

In summary, the Mo vacancies were successfully introduced into MoP by a facile acid etching treatment on Co$_2$P/MoP heterostructures, leading to porous structures as well as surface electronic modulation, which accelerated the mass transfer, and exposed abundant highly active P sites for the activity improvement towards HER. Especially, both the experiments and DFT calculation results confirmed the surface electron redistribution resulting from Mo vacancies, and more electrons transfer to P sites and result in the increased valance electron concentration around E_F, making the exposed P sites serve as ideal catalytic

sites for hydrogen evolution with a ΔG_{H*} close to zero. Meanwhile, an IPF from terminal Mo atoms to exposed P atoms can offer a more efficient "H delivery" mechanism than pristine MoP, which enabled higher surface H coverages as well as corresponding faster Heyrovsky reaction kinetics. As expected, the Mov-MoP electrocatalyst showed accelerated HER kinetics with an ultralow Tafel slope (41 mV dec^{-1}) as well as a wide current density range (until 100 mA cm^{-2}) of Volmer-Heyrovsky mechanism, achieving ultrafast current density growth and ultimately exceeding the commercial Pt/C catalyst for high-efficiency hydrogen evolution. More importantly, we first reported the P p-band center could be used as an alternative descriptor to evaluate the HER performance of the electrocatalysts utilizing P atoms as main active sites. Furthermore, this work also demonstrates that metal vacancies provide an effective tactic to optimize catalytic activity for metal compound-based electrocatalysts.

CRediT authorship contribution statement

Ting Guo: Investigation, Data curation, Visualization, Writing – original draft. **Hao Fei:** Formal analysis. **Ruoqi Liu:** Software, Formal analysis. **Fangyang Liu:** Writing – review & editing. **Dezhi Wang:** Writing – review & editing, Supervision. **Zhuangzhi Wu:** Conceptualization, Writing – review & editing, Supervision.

Declaration of Competing Interest

The authors declare that they have no known competing financial interests or personal relationships that could have appeared to influence the work reported in this paper.

Data availability

Data will be made available on request.

Acknowledgements

Appendix A. Supporting information

Supplementary data associated with this article can be found in the online version at doi:10.1016/j.apcatb.2023.123480.

References

[1] X. Wang, Y. Zhang, H. Si, Q. Zhang, J. Wu, L. Gao, X. Wei, Y. Sun, Q. Liao, Z. Zhang, K. Ammarah, L. Gu, Z. Kang, Y. Zhang, Single-atom vacancy defect to trigger high-efficiency hydrogen evolution of MoS2, J. Am. Chem. Soc. 142 (2020) 4298–4308, https://doi.org/10.1021/jacs.9b12113.

[2] Y. Li, W. Wang, M. Cheng, Y. Feng, X. Han, Q. Qian, Y. Zhu, G. Zhang, Arming Ru with oxygen-vacancy-enriched RuO2 sub-nanometer skin activates superior bifunctionality for pH-universal overall water splitting, Adv. Mater. 35 (2023), 2206351, https://doi.org/10.1002/adma.202206351.

[3] F. Bai, L. Xu, X. Zhai, X. Chen, W. Yang, Vacancy in ultrathin 2D nanomaterials toward sustainable energy application, Adv. Energy Mater. 10 (2020), 1902107, https://doi.org/10.1002/aenm.201902107.

[4] Y. Ma, M. Chen, H. Geng, H. Dong, P. Wu, X. Li, G. Guan, T. Wang, Synergistically tuning electronic structure of porous beta-Mo2C spheres by co doping and Mo-vacancies defect engineering for optimizing hydrogen evolution reaction activity, Adv. Funct. Mater. 30 (2020), 2000561, https://doi.org/10.1002/adfm.202000561.

[5] X. Wang, J. Ding, W. Song, X. Yang, T. Zhang, Z. Huang, H. Wang, X. Han, W. Hu, Cation vacancy clusters in Ti3C2Tx MXene induce ultra-strong interaction with noble metal clusters for efficient electrocatalytic hydrogen evolution, Adv. Energy Mater. 13 (2023), 2300148, https://doi.org/10.1002/aenm.202300148.

[6] Y. Zhang, R. Lu, C. Wang, Y. Zhao, L. Qi, Electronic and vacancy engineering of Mo-RuCoOx nanoarrays for high-efficiency water splitting, Adv. Funct. Mater. (2023), 2303073, https://doi.org/10.1002/adfm.202303073.

[7] J. Xie, H. Zhang, S. Li, R. Wang, X. Sun, M. Zhou, J. Zhou, X.W. Lou, Y. Xie, Defect-rich MoS2 ultrathin nanosheets with additional active edge sites for enhanced electrocatalytic hydrogen evolution, Adv. Mater. 25 (2013) 5807, https://doi.org/10.1002/adma.201302685.

[8] P. Zeng, Y. Meng, Z. Liu, G.-Q. Sun, X.-Y. Li, X.-Y. Yang, C.-F. Ye, Y. Li, J.-P. Liu, L.-H. Chen, B.-L. Su, Y.-L. Wang, N-doping coupled with co-vacancies activating sulfur atoms and narrowing bandgap for CoS toward synergistically accelerating hydrogen evolution, Small (2023), 2301279, https://doi.org/10.1002/smll.202301279.

[9] N. Yao, R. Meng, F. Wu, Z. Fan, G. Cheng, W. Luo, Oxygen-vacancy-induced CeO2/Co4N heterostructures toward enhanced pH-Universal hydrogen evolution reactions, Appl. Catal. B Environ. 277 (2020), 119282, https://doi.org/10.1016/j.apcatb.2020.119282.

[10] H. Li, C. Tsai, A.L. Koh, L. Cai, A.W. Contryman, A.H. Fragapane, J. Zhao, H.S. Han, H.C. Manoharan, F. Abild-Pedersen, J.K. Norskov, X. Zheng, Activating and optimizing MoS2 basal planes for hydrogen evolution through the formation of strained sulphur vacancies, Nat. Mater. 15 (2016) 48, https://doi.org/10.1038/NMAT4465.

[11] C.-F. Li, J.-W. Zhao, L.-J. Xie, J.-Q. Wu, G.-R. Li, Fe doping and oxygen vacancy modulated Fe-Ni5P4/NiFeOH nanosheets as bifunctional electrocatalysts for efficient overall water splitting, Appl. Catal. B Environ. 291 (2021), 119987, https://doi.org/10.1016/j.apcatb.2021.119987.

[12] B. Liu, B. He, H.-Q. Peng, Y. Zhao, J. Cheng, J. Xia, J. Shen, T.-W. Ng, X. Meng, C.-S. Lee, W. Zhang, Unconventional nickel nitride enriched with nitrogen vacancies as a high-efficiency electrocatalyst for hydrogen evolution, Adv. Sci. 5 (2018), 1800406, https://doi.org/10.1002/advs.201800406.

[13] S. Liu, C. Chen, Y. Zhang, Q. Zheng, S. Zhang, X. Mu, C. Chen, J. Ma, S. Mu, Vacancy-coordinated hydrogen evolution reaction on MoO3−x anchored atomically dispersed MoRu pairs, J. Mater. Chem. A 7 (2019) 14466–14472, https://doi.org/10.1039/c9ta03719e.

[14] F. Li, X. Zhao, J. Mahmood, M.S. Okyay, S.-M. Jung, I. Ahmad, S.-J. Kim, G.-F. Han, N. Park, J.-B. Baek, Macroporous inverse Opal-like MoxC with incorporated Mo vacancies for significantly enhanced hydrogen evolution, ACS Nano 11 (2017) 7527–7533, https://doi.org/10.1021/acsnano.7b04205.

[15] S. Park, J. Park, H. Abroshan, L. Zhang, J.K. Kim, J. Zhang, J. Guo, S. Siahrostami, X. Zheng, Enhancing catalytic activity of mos2 basal plane S-vacancy by Co cluster addition, ACS Energy Lett. 3 (2018) 2685–2693, https://doi.org/10.1021/acsenergylett.8b01567.

[16] Y.-R. Zheng, P. Wu, M.-R. Gao, X.-L. Zhang, F.-Y. Gao, H.-X. Ju, R. Wu, Q. Gao, R. You, W.-X. Huang, S.-J. Liu, S.-W. Hu, J. Zhu, Z. Li, S.-H. Yu, Doping-induced structural phase transition in cobalt diselenide enables enhanced hydrogen evolution catalysis, Nat. Commun. 9 (2018), 2533, https://doi.org/10.1038/s41467-018-04954-7.

[17] W. Wu, C. Niu, C. Wei, Y. Jia, C. Li, Q. Xu, Activation of MoS2 basal planes for hydrogen evolution by zinc, Angew. Chem. Int. Ed. 58 (2019) 2029–2033, https://doi.org/10.1002/anie.201812475.

[18] W. Zhong, Z. Wang, N. Gao, L. Huang, Z. Lin, Y. Liu, F. Meng, J. Deng, S. Jin, Q. Zhang, L. Gu, Coupled vacancy pairs in Ni-doped CoSe for improved electrocatalytic hydrogen production through topochemical deintercalation, Angew. Chem. Int. Ed. 59 (2020) 22743–22748, https://doi.org/10.1002/anie.202011378.

[19] Z. Luo, R. Miao, T.D. Huan, I.M. Mosa, A.S. Poyraz, W. Zhong, J.E. Cloud, D.A. Kriz, S. Thanneeru, J. He, Y. Zhang, R. Ramprasad, S.L. Suib, Mesoporous MoO3−x material as an efficient electrocatalyst for hydrogen evolution reactions, Adv. Energy Mater. 6 (2016), 1600528, https://doi.org/10.1002/aenm.201600528.

[20] X. Zhang, F. Zhou, W. Pan, Y. Liang, R. Wang, General construction of molybdenum-based nanowire arrays for pH-universal hydrogen evolution electrocatalysis, Adv. Funct. Mater. 28 (2018), 1804600, https://doi.org/10.1002/adfm.201804600.

[21] P. Xiao, M.A. Sk, L. Thia, X. Ge, R.J. Lim, J.-Y. Wang, K.H. Lim, X. Wang, Molybdenum phosphide as an efficient electrocatalyst for the hydrogen evolution reaction, Energy Environ. Sci. 7 (2014) 2624–2629, https://doi.org/10.1039/C4EE00957F.

[22] J. Zhao, Q. Wu, M. Wen, Temperature-controlled assembly and morphology conversion of CoMoO4·3/4H2O nano-superstructured grating materials, J. Mater. Sci. 44 (2009) 6356–6362, https://doi.org/10.1007/s10853-009-3876-y.

[23] Y. Men, P. Li, J. Zhou, G. Cheng, S. Chen, W. Luo, Tailoring the electronic structure of Co2P by N doping for boosting hydrogen evolution reaction at all pH values, ACS Catal. 9 (2019) 3744–3752, https://doi.org/10.1021/acscatal.9b00407.

[24] M. Hu, B. Liu, H. Chen, X. Xu, P. Jing, X. Guo, R. Yang, X. Wang, R. Gao, J. Zhang, Universal construction of sulfur doped molybdenum-based nanosheets for enhanced hydrogen evolution in a wide pH range, Appl. Catal. B Environ. 322 (2023), 122131, https://doi.org/10.1016/j.apcatb.2022.122131.

[25] X. Zhang, Z. Wu, D. Wang, Oxygen-incorporated defect-rich MoP for highly efficient hydrogen production in both acidic and alkaline media, Electrochim. Acta 281 (2018) 540–548, https://doi.org/10.1016/j.electacta.2018.05.176.

[26] Y. Zhu, W. Zhou, J. Yu, Y. Chen, M. Liu, Z. Shao, Enhancing electrocatalytic activity of perovskite oxides by tuning cation deficiency for oxygen reduction and evolution reactions, Chem. Mater. 28 (2016) 1691–1697, https://doi.org/10.1021/acs.chemmater.5b04457.

[27] C. Deng, F. Ding, X. Li, Y. Guo, W. Ni, H. Yan, K. Sun, Y.-M. Yan, Templated-preparation of a three-dimensional molybdenum phosphide sponge as a high performance electrode for hydrogen evolution, J. Mater. Chem. A 4 (2016) 59–66, https://doi.org/10.1039/C5TA05453B.

[28] S. Li, Z. Geng, X. Wang, X. Ren, J. Liu, X. Hou, Y. Sun, W. Zhang, K. Huang, S. Feng, Optimizing the surface state of cobalt-iron bimetallic phosphide via regulating phosphorus vacancies, Chem. Commun. 56 (2020) 2602–2605, https://doi.org/10.1039/C9CC09741D.

[29] W. Zhu, C. Tang, D. Liu, J. Wang, A.M. Asiri, X. Sun, A self-standing nanoporous MoP$_2$ nanosheet array: an advanced pH-universal catalytic electrode for the hydrogen evolution reaction, J. Mater. Chem. A 4 (2016) 7169–7173, https://doi.org/10.1039/C6TA01328G.

[30] Y. Shi, Y. Zhou, D.-R. Yang, W.-X. Xu, C. Wang, F.-B. Wang, J.-J. Xu, X.-H. Xia, H.-Y. Chen, Energy level engineering of MoS$_2$ by transition-metal doping for accelerating hydrogen evolution reaction, J. Am. Chem. Soc. 139 (2017) 15479–15485, https://doi.org/10.1021/jacs.7b08881.

[31] X. Zhang, T. Liu, T. Guo, Z. Mu, X. Hu, K. He, X. Chen, V.P. Dravid, Z. Wu, D. Wang, High-performance MoC electrocatalyst for hydrogen evolution reaction enabled by surface sulfur substitution, ACS Appl. Mater. Interfaces 13 (2021) 40705–40712, https://doi.org/10.1021/acsami.1c12143.

[32] W. Liu, X. Wang, F. Wang, K. Du, Z. Zhang, Y. Guo, H. Yin, D. Wang, A durable and pH-universal self-standing MoC–Mo$_2$C heterojunction electrode for efficient hydrogen evolution reaction, Nat. Commun. 12 (2021), 6776, https://doi.org/10.1038/s41467-021-27118-6.

[33] F. Tang, W. Cheng, Y. Huang, H. Su, T. Yao, Q. Liu, J. Liu, F. Hu, Y. Jiang, Z. Sun, S. Wei, Strong surface hydrophilicity in co-based electrocatalysts for water oxidation, ACS Appl. Mater. Interfaces 7 (2017), https://doi.org/10.1021/acsami.7b07088.

[34] A.B.D. Cassie, S. Baxter, Wettability of porous surfaces, Trans. Faraday Soc. 40 (1944) 546, https://doi.org/10.1039/tf9444000546.

[35] P.D. Tran, T.V. Tran, M. Orio, S. Torelli, Q.D. Truong, K. Nayuki, Y. Sasaki, S. Y. Chiam, R. Yi, I. Honma, J. Barber, V. Artero, Coordination polymer structure and revisited hydrogen evolution catalytic mechanism for amorphous molybdenum sulfide, Nat. Mater. 15 (2016) 640–646, https://doi.org/10.1038/nmat4588.

[36] J. Jia, W. Zhou, G. Li, L. Yang, Z. Wei, L. Cao, Y. Wu, K. Zhou, S. Chen, Regulated synthesis of Mo sheets and their derivative MoX sheets (X: P, S, or C) as efficient electrocatalysts for hydrogen evolution reactions, ACS Appl. Mater. Interfaces 9 (2017) 8041–8046, https://doi.org/10.1021/acsami.6b12103.

[37] S. Gao, Y. Liu, G.-D. Li, Y. Guo, Y. Zou, X. Zou, General urea-assisted synthesis of carbon-coated metal phosphide nanoparticles for efficient hydrogen evolution electrocatalysis, Electrochim. Acta 199 (2016) 99–107, https://doi.org/10.1016/j.electacta.2016.03.104.

[38] S. Shen, Z. Wang, Z. Lin, K. Song, Q. Zhang, F. Meng, L. Gu, W. Zhong, Crystalline-amorphous interfaces coupling of CoSe$_2$/CoP with optimized d-band center and boosted electrocatalytic hydrogen evolution, Adv. Mater. 34 (2022), 2110631, https://doi.org/10.1002/adma.202110631.

[39] T. Shinagawa, A.T. Garcia-Esparza, K. Takanabe, Insight on Tafel slopes from a microkinetic analysis of aqueous electrocatalysis for energy conversion, Sci. Rep. 5 (2015), 13801, https://doi.org/10.1038/srep13801.

[40] J. Sun, W. Xu, C. Lv, L. Zhang, M. Shakouri, Y. Peng, Q. Wang, X. Yang, D. Yuan, M. Huang, D. Yang, L. Zhang, Co/MoN hetero-interface nanoflake array with enhanced water dissociation capability achieves the Pt-like hydrogen evolution catalytic performance, Appl. Catal. B-Environ. 286 (2021), 119882, https://doi.org/10.1016/j.apcatb.2021.119882.

[41] B. Hammer, J.K. Norskov, Why gold is the noblest of all the metals, Nature 376 (1995) 238–240, https://doi.org/10.1038/376238a0.

[42] J.K. Nørskov, T. Bligaard, J. Rossmeisl, C.H. Christensen, Towards the computational design of solid catalysts, Nat. Chem. 1 (2009) 37–46, https://doi.org/10.1038/nchem.121.

[43] A. Grimaud, K.J. May, C.E. Carlton, Y.-L. Lee, M. Risch, W.T. Hong, J. Zhou, Y. Shao-Horn, Double perovskites as a family of highly active catalysts for oxygen evolution in alkaline solution, Nat. Commun. 4 (2013), 2439, https://doi.org/10.1038/ncomms3439.

[44] Y. Zhou, S. Sun, J. Song, S. Xi, B. Chen, Y. Du, A.C. Fisher, F. Cheng, X. Wang, H. Zhang, Z.J. Xu, Enlarged Co-O covalency in octahedral sites leading to highly efficient spinel oxides for oxygen evolution reaction, Adv. Mater. 30 (2018), 1802912, https://doi.org/10.1002/adma.201802912.

[45] J. Wang, Z. Zhang, H. Song, B. Zhang, J. Liu, X. Shai, L. Miao, WateR Dissociation Kinetic-oriented Design of Nickel Sulfides Via Tailored Dual Sites for Efficient Alkaline Hydrogen Evolution, Adv. Funct. Mater. 31 (2021), 2008578, https://doi.org/10.1002/adfm.202008578.

[46] J. Wang, X. Li, B. Wei, R. Sun, W. Yu, H.Y. Hoh, H. Xu, J. Li, X. Ge, Z. Chen, C. Su, Z. Wang, Activating basal planes of NiPS$_3$ for hydrogen evolution by nonmetal heteroatom doping, Adv. Funct. Mater. 30 (2020), 1908708, https://doi.org/10.1002/adfm.201908708.

[47] Y. Zhang, H. Lei, D. Duan, E. Villota, C. Liu, R. Ruan, New insight into the mechanism of the hydrogen evolution reaction on MoP(001) from first principles, ACS Appl. Mater. Interfaces 10 (2018) 20429–20439, https://doi.org/10.1021/acsami.8b03976.

[48] Y. Liu, Y. Chen, Y. Tian, T. Sakthivel, H. Liu, S. Guo, H. Zeng, Z. Dai, Synergizing hydrogen spillover and deprotonation by the internal polarization field in a MoS$_2$/NiPS$_3$ vertical heterostructure for boosted water electrolysis, Adv. Mater. 34 (2022), 2203615, https://doi.org/10.1002/adma.202203615.

[49] W. Fu, Y. Wang, W. Tian, H. Zhang, J. Li, S. Wang, Y. Wang, Non-metal single-phosphorus-atom catalysis of hydrogen evolution, Angew. Chem. Int. Ed. 59 (2020) 23791–23799, https://doi.org/10.1002/anie.202011358.